ACS APPLIED MATERIALS & INTERFACES

Research Article

www.acsami.org

Biomimetic Spiral-Cylindrical Scaffold Based on Hybrid Chitosan/Cellulose/Nano-Hydroxyapatite Membrane for Bone Regeneration

Hong Jiang,[†] Yi Zuo,[‡] Qin Zou,[‡] Huanan Wang,[‡] Jingjing Du,[‡] Yubao Li,*[,‡] and Xiaochao Yang*[,†]

[†]Department of Biomedical Materials Science, School of Biomedical Engineering, Third Military Medical University, Chongqing 400038, P. R. China

[‡]Research Center for Nano Biomaterials, Analytical and Testing Center, Sichuan University, Chengdu 610064, P. R. China

Supporting Information

ABSTRACT: Natural bone is a complex material with well-designed architecture. To achieve successful bone integration and regeneration, the constituent and structure of bone-repairing scaffolds need to be functionalized synergistically based on biomimetics. In this study, a hybrid membrane composed of chitosan (CS), sodium carboxymethyl cellulose (CMC), and nano-hydroxyapatite (n-HA) was curled in a concentric manner to generate an anisotropic spiral-cylindrical scaffold, with compositional and structural properties mimicking natural bone. After optimization in terms of morphology, hydrophilicity, swelling and degradation pattern, the osteoblast cells seeded on the membrane of 60 wt% n-HA exhibited the highest cell viability and osteocalcin expression. In vivo osteogenesis assessment revealed that the spiral-cylindrical architecture played a dominant role in bone regeneration and osseointegration. Newly formed bone tissue grew through the longitudinal direction of the cylinder-shaped scaffold bridging both ends of the defect, bone marrow penetrated the entire scaffold and formed a medullary cavity in the center of the spiral cylinder. This study for the first time demonstrates that the spiral-cylindrical scaffold can promote complete infiltration of bone tissues in vivo, leading to successful osteointegration and functional reconstruction of bone defects. It suggests that the biomimetic spiral-cylindrical scaffold could be a promising candidate for bone regeneration applications.

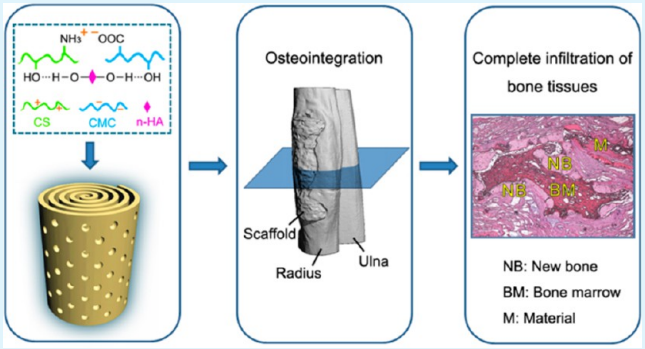

KEYWORDS: *biomimetic, spiral-cylindrical scaffold, osteointegration, bone regeneration*

1. INTRODUCTION

Bone repair represents a major research focus of bone defects resulting from injuries, malformation, osteoporosis, and tumor surgery.[1] For large bone defects, bulk scaffolds are preferred to other forms of materials (such as cements, injectable gels, and membranes[2−5]) because of their capability of filling the missing segments and provide sufficient temporary mechanical support for host bone immediately after implantation.[6] However, to achieve successful bone regeneration, the constituent and structure of the scaffold need to be functionalized synergistically. Despite the hard endeavors in this field, a very few scaffolds succeeded in completely bone integration and functional reconstruction in vivo.[7]

Natural bone is an anisotropic complex material that mainly composed of cells, collagen matrix, and calcium phosphate in the form of hydroxyapatite (HA). Inspired by the constituents of the natural bone, a number of studies have used organic−inorganic compounds to fabricate bone-repairing scaffolds.[8−11] Among various classes of polymeric materials, polysaccharides (chitosan, cellulose, alginate, etc.) possess several inherent advantages: biodegradability, noncytotoxicity, low immunogenicity, good biocompatibility, as well as abundant renewable recources.[12,13] They have been extensively used as polymer matrix of organic−inorganic composite materials in recent years, such as hydroxyapatite-containing chitosan nanofibers, hydroxyapatite/bacterial cellulose nanocomposites, and calcium phosphate-alginate hydrogels.[14−16] On the other hand, the structure of the scaffold plays another critical role in the reconstruction of bone tissues, of which a highly porous structure is identified as being critical for bone ingrowth, as well as necessary nutrient and waste transport.[17,18] However, the past decades have witnessed limited success for the use of porous scaffolds for the treatment of large bone defects, the primary reason for this is the limitation of bone ingrowth.[19−21] Unlike the anisotropy of natural bone, conventional porous scaffolds exhibit isotropic transmission characteristics of stress,[22] which hampers their integration with the host bone. Accordingly, finely designed 3D scaffolds with similar structures of natural bone are required for better bone integration.

In recent work, we reported a hybrid CS/CMC/n-HA membrane prepared by gradual electrostatic assembly.[23] Natural biodegradable polysaccharides, cationic CS and anionic

Received: September 6, 2013
Accepted: November 5, 2013
Published: November 5, 2013

CMC, together with inorganic phase of n-HA were integrated to generate a hybrid membrane with organic-inorganic constituents similar to that of natural bone. Opposite charged CS-CMC polysaccharides assembled through electrostatic interaction to form the membrane framework, while n-HA crystals filled in the polymer matrices with hydrogen bonds to make a uniform distribution. Herein, an anisotropic spiral-cylindrical scaffold with similar structure of natural bone was developed based on the hybrid membrane, aiming at promoting complete infiltration of bone tissue throughout the entire scaffold and eventually achieving bone integration and functional reconstruction. Similar structures were also found in the literatures, such as microchannel structure reported by Zuo et al.,[24] orienting nanofiber matrices studied by Deng et al.[25] and spiral nanofibrous scaffolds prepared by Wang et al.[26−28] These studies confirmed that osteon-like structures have the potential promotion of cell attachment, migration, proliferation and differentiation during in vitro culture; however, in vivo osteointegration of these scaffolds has not been proved. In this study, physicochemical characteristics, degradation behaviour, and cellular compatibility of the hybrid membranes were assessed prior to scaffold fabrication. The optimized membrane was perforated and curled in a concentric manner to generate an anisotropic spiral-cylindrical scaffold. To investigate the in vivo osteogenesis capability, the scaffolds were implanted into radius defects of New Zealand white rabbits. Osteogenesis assessment was carried out by means of X-ray photography, microcomputed tomography (micro-CT), and histological analysis with hematoxylin and eosin (H&E) staining.

2. EXPERIMENTAL SECTION

2.1. Preparation of the Hybrid Membranes. The hybrid membranes were prepared by gradual electrostatic assembly according to our early work.[23] The chemical interaction among the three components was confirmed by FT-IR and XRD in the previous work, and the preparation parameters of the hybrid membrane were optimized according to their mechanical properties. On the basis of this, the mass ratio between CS and CMC was fixed at 1:1, membranes with different n-HA ratio were used for further assessment. The hybrid membranes containing 0, 20, 40, and 60 wt % of n-HA were listed as **M0**, **M20**, **M40**, and **M60** respectively. Membranes with n-HA ratio higher than 60 wt % were too fragile for practical application which were not used in this study.

2.2. Characterization of the Hybrid Membranes. *2.2.1. Macroscopic Observation.* The macroscopic observation of membranes in the wet state was recorded by digital camera (EOS600D, Canon, Japan).

2.2.2. Water-Contact Angle. Water-contact angle experiments of the dry membranes were performed using a contact angle meter (JC2000C, Zhongchen, China) at room temperature.

2.2.3. Swelling. The swelling behavior of the membranes was determined in deionized water using a gravimetric method. The dry membranes of known weight (W_d) were immersed in deionized water at 37 ± 0.1°C for 48 h, and the wet weight (W_w) was determined by wiping off the surface water with filter paper. The swelling degree (SD) of the membrane was calculated according to the following equation: SD (%) = $(W_w - W_d)/W_d \times 100$.

2.3. Degradation of the Hybrid Membranes. The in vitro and in vivo degradation behaviors of the hybrid membranes (**M0**, **M20**, **M40**, and **M60**) were investigated. Pure CS membrane (symbolized as CS) prepared under the same conditions was used as a control. The in vitro biodegradation were examined by soaking the membranes in phosphate buffer solution (PBS, pH = 7.4, changed once a week), 37 ± 0.1°C water bath and 150 rpm permanent shaking to mimic a typical physiological condition. For the in vivo biodegradation, the membranes were intramuscularly implanted into back muscles of Sprague−Dawley (SD) rats. All animal experimental procedures were approved by the Ethic Committee of West China Hospital, Sichuan University. The samples were collected at 1, 4, 8, and 12 week time intervals. Before test, the in vivo samples were immersed in a 0.25% trypsin solution at 37 °C for 24 h to digest the tissues attached on the membranes after implantation. Non-implanted control samples were subjected to the same conditions, indicating that the trypsin did not degrade the membranes. Then both the in vitro and in vivo samples were fully rinsed with deionized water and air-dried at room temperature.

2.3.1. Scanning Electron Microscopy (SEM) and Energy Dispersive X-Ray Spectroscopy (EDS) Analysis. The surface morphologies of the membranes and the distribution of n-HA particles were characterized by SEM (JSM-6510LV, JEOL, Japan) and EDS (INCA Energy 250, Oxford, Britain) area scan at 20 kV after surface gold sputtering.

2.3.2. Weight Loss. The degradation rate of the membranes was examined with respect to weight loss: Weight loss (%) = $(W_o - W_r) \times 100/W_o$, where W_o and W_r represent the weight of the dried membrane before and after degradation respectively.

2.3.3. Roasting Test. The n-HA ratio of residual hybrid membranes at different degradation time were measured by roasting test. The membranes (**M20**, **M40**, and **M60**) were roasted in muffle furnace at 1000 °C for 2 h to burn out polysaccharides, and the remaining weight was from heat stable n-HA. Three samples were tested in parallel for each membrane.

2.4. Cellular Compatibility of the Hybrid Membranes. Primary osteoblast cells were obtained from the calvarias of 3-day-old SD rats according to established procedure.[29−31] Immunocytochemistry and mineralized nodule formation test were used to identify the cell phenotype (see the Supporting Information, Figure S1). Osteoblasts at the third passage were used in the experiments. The hybrid membranes (**M0**, **M20**, **M40**, and **M60**) were tailored into disk-shaped slices (thickness ≈ 300 μm, diameter ≈ 13 mm). After sterilization with 75% ethanol and washing with distilled water, the membranes were seeded with osteoblasts (2×10^4 cells/well) in 24-well plates. The cells were cultured with Ham's F-12 medium (Gibco, U.S.A., 1 mL/well) in humidified incubator (37°C, 5% CO_2).

2.4.1. Morphology. The morphology and spreading of osteoblasts growing on the membranes were observed with SEM (JSM-6510LV, JEOL, Japan) and fluorescence microscopy (TE2000-U, Nikon Eclipse, Japan). Before SEM observation, the samples were rinsed with PBS, fixed with 2.5 vol. % glutaraldehyde, dehydrated through graded ethanol and critical point dried in CO_2. For the fluorescence observation, the cells were labelled with the red fluorescent dye DiI (Beyotime Institute of Biotechnology, China) before seeding.

2.4.2. Proliferation. The proliferation of osteoblasts cultured with membranes was measured by MTT (3-[4,5-dimethylthiazol-2-yl]-2,5-diphenyl-2*H*-tetrazolium bromide, Amresco, U.S.A.) assay with a multilabel counter (Wallac Victor3 1420, Perkin-Elmer Co., U.S.A.) at 490 nm.

2.4.3. Differentiation. The osteocalcin (OCN) content was measured in the culture medium using the rat bone gla protein/osteocalcin (BGP/OCN) ELISA kit (RapidBio Lab, U.S.A.) according to the manufacturer's protocol.

2.5. Preparation and Characterization of the Membrane-Based Spiral-Cylindrical Scaffold. The CS/CMC/n-HA hybrid membrane with 60 wt % n-HA (**M60**) was used for scaffold fabrication. An anisotropic spiral-cylindrical scaffold was designed to simulate the microstructure of natural bone (Figure 1). To achieve better bone ingrowth, the membrane (thickness ≈ 300 μm) was treated by mechanical perforation, with a pore size of 300 μm and a pitch (pore-to-pore spacing) of 1.0 mm. Then, the perforated membrane was closely curled in a concentric manner to form a column with a spiral cross-section, the skirt was eroded by acetic acid solution and cemented on the scaffold (Figure 2a). The size of the scaffold can be regulated according to the membrane size.

The compressive strength of the scaffold was characterized by universal mechanical testing machine (RGT-5A 5KN, Shenzhen Reger

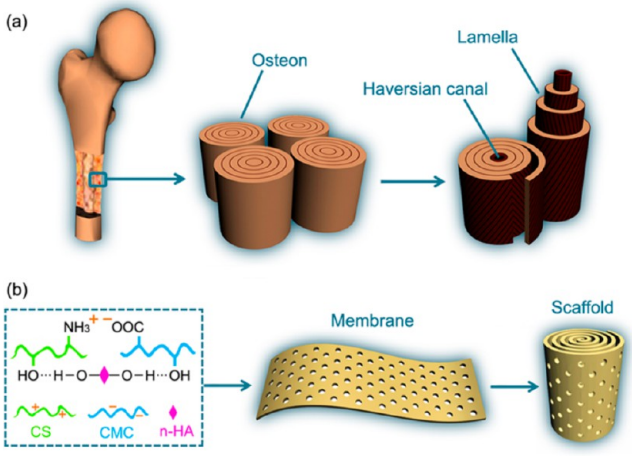

Figure 1. (a) Microstructure of natural bone and (b) fabrication process of biomimetic spiral-cylindrical scaffold based on the hybrid CS/CMC/n-HA membrane.

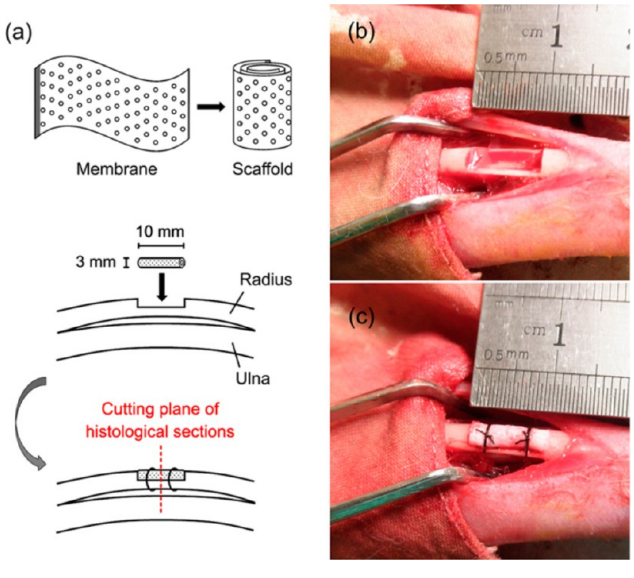

Figure 2. (a) Schematic diagram of surgical procedures, (b) concave defect of rabbit radius, and (c) implantation and fixation of the scaffold.

Instrument Co., China). The cylindrical scaffold was prepared with a size of Φ8 × 16 mm. Three parallel samples were tested with a cross-head speed of 1.0 mm/min until 40% reduction in specimen height.

2.6. In Vivo Osteogenesis Assessment of the Spiral-Cylindrical Scaffold. The animal experiments were approved by the Ethic Committee of West China Hospital, Sichuan University. The spiral-cylindrical scaffolds were adjusted to 10 mm in length and 3 mm in diameter for the designed animal model. Eighteen New Zealand white rabbits (2.0–2.5 kg) were divided into the scaffold group (9) and the control group (9). Rabbits were anesthetized with intravenous sodium pentobarbital (30 mg/kg body weight) before surgery. Then a concave defect (10 mm long, 3 mm deep) was created at the middle segment of the left radius (Figure 2b). After the debris at defect site was washed away by physiological saline solution, the defect was filled with the spiral-cylindrical scaffold, fixed by stitches (Figure 2c). The control group was operated without implantation. Animals were sacrificed at 4, 8, and 12 weeks post-operation for assessment (3 samples for each time point and each group).

2.6.1. X-ray Photography. The mineralization and osteogenesis of radius defects were evaluated with high-resolution digital radiography system (Elitys, Trophy Radiologie Inc, France), operating at 60 kV, 4 mA, and 0.06 s for exposure.

2.6.2. Microcomputed Tomography (Micro-CT). Three-dimensional (3D) analysis was conducted on the rabbit bone specimens using a micro-CT imaging system (μCT80 scanner, Scanco Medical, Switzerland). The scanning system was set to 55 kV, 145 μA, a total of 700 microtomographic slices with a slice increment of 25 μm were taken for each sample. A threshold between 200 and 1000 was applied to discriminate bone from other tissue, and 3D Gaussian filter was constrained at σ = 1.2 and support = 2 for partial suppression of the noise in the volumes. The 3D reconstructed images were acquired from a series of 650 serial 2048 × 2048 bitmap images. For the quantitative evaluation of osteogenesis inside the scaffold, a cylindrical region of interest (ROI) with a diameter of 3 mm and a height of 10 mm was chosen to represent the spiral-cylindrical scaffold and the inner regenerated bone.

2.6.3. Histological Analysis. For the histological analysis, rabbit bone specimens (only for the scaffold group) were fixed in 10% neutral formalin, decalcified with EDTA, gradient-dehydrated with ethanol and embedded in paraffin. Histological cross sections (5 μm thick) were made in the middle part of the cylindrical scaffold, which were perpendicular to the long axis of the radius, as shown in Figure 2a (the dotted line). The sections were stained with hematoxylin and eosin (H&E, Solarbio, China) and observed by optical microscopy (TE2000-U, Nikon Eclipse, Japan).

2.7. Statistical Analysis. Quantitative data were presented as means ± standard deviation (SD). Statistical analysis was carried out using one-way ANOVA with a Student–Newman–Keuls test. A significant difference was considered when $p < 0.05$.

3. RESULTS

3.1. Physicochemical Properties of the Hybrid Membranes. Figure 3a exhibited the macroscopic morphology

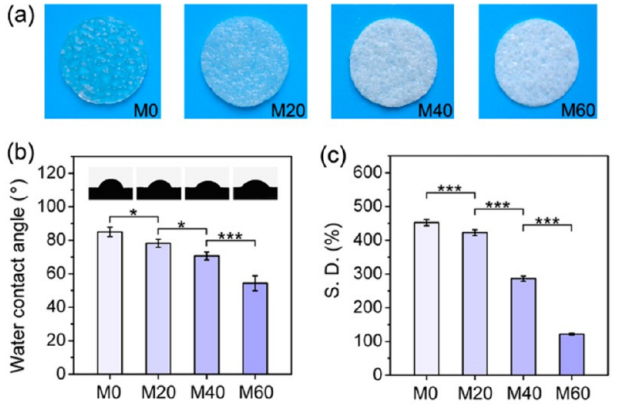

Figure 3. (a) Macrographs, (b) water contact angle, and (c) swelling degree (S.D.) of the hybrid membranes. (Error bars represent standard deviation from the mean (n = 3). ***: p<0.001. *: p<0.05.)

of the membranes. With the increase of n-HA, the membrane changed its appearance from transparent to dense quality, accompanying with the increase of surface roughness. Moreover, both of the water contact angle and swelling degree decreased with the increase of n-HA ratio in the membrane, as shown in Figure 3b and c.

3.2. Degradation Behavior of the Hybrid Membranes. The surface morphologies of the membranes before and after 12 weeks of in vitro and in vivo degradation were shown in Figure 4. The CS membrane exhibited a smooth surface, little morphology change was observed implying its slow degradation rate. However, irregular ridges and visual defects were observed on all the hybrid membrane surface after degradation. Except

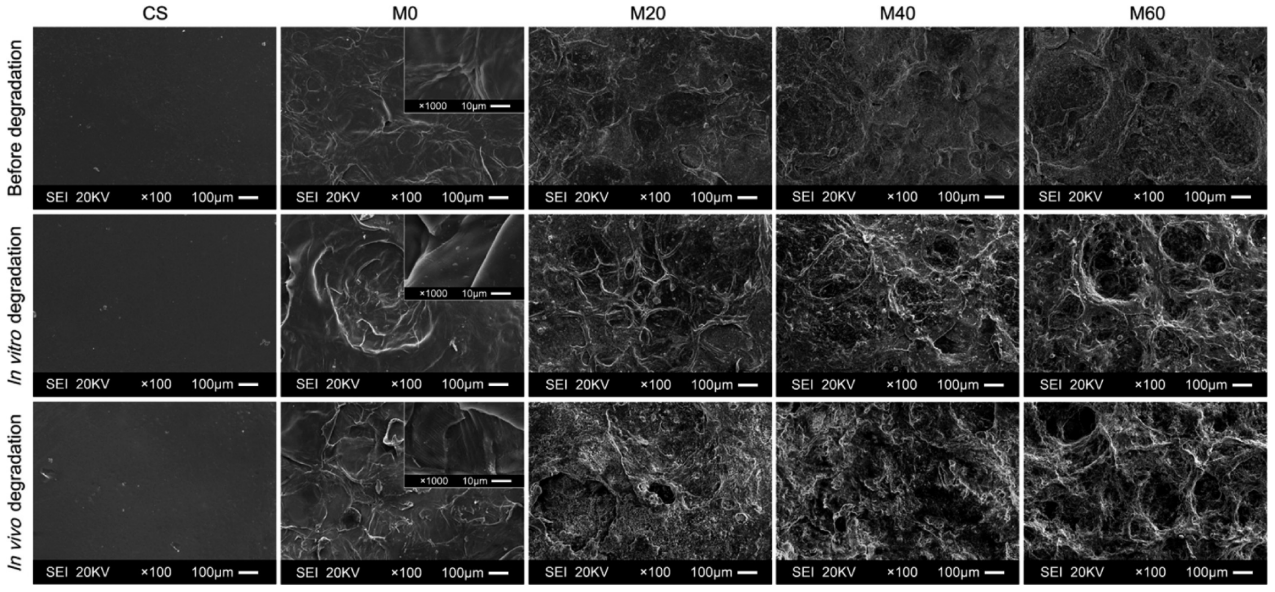

Figure 4. SEM photographs of the surface morphologies of different membranes before and after 12 weeks in vitro/in vivo degradation.

for craters and ridges of **M0**, some visual holes appeared on **M20**, **M40**, and **M60** because of the degradation of polysaccharides. Irregular holes with size of 100−300 μm in diameter were observed on **M60**. EDS area scan showed that calcium (Ca) and phosphorus (P) are uniformly distributed in all the CS/CMC/n-HA membranes before and after in vitro/in vivo degradation (data not shown). This indicated that the distribution of n-HA particles was uniform in polysaccharide matrix after degradation. According to SEM observation, the porosity of degraded scaffold was higher in in vivo experiments when compared to that of in vitro experiments. Morphology changes implied that the in vivo degradation level was higher than in vitro for all the membranes, these results were further confirmed by the weight loss. Data showed that the in vivo weight loss level was around 2 times of the in vitro level. As can be seen from Figure 5, the weight loss of CS membrane was very low. For the hybrid membranes, the initial weight loss decreased with the increase of n-HA ratio. But several weeks later, the weight loss of **M60** became higher than **M20** and **M40** while still much lower than **M0** which containing no inorganic n-HA. This phenomenon was similarly observed in both in vitro and in vivo degradation process. To check if n-HA diffused into the surrounding environment, roasting test was run at different time intervals. The n-HA ratio of the residual hybrid membranes remained unchanged throughout the whole degradation process (data not shown).

3.3. Cellular Compatibility of the Hybrid Membranes.

The morphology of osteoblast cells growing on the hybrid membranes was shown in Figure 6a and b. The cells on **M0** exhibited an elongated shape and limited intercellular communication, probably because the smooth surface was unfavorable for cell adhension.[32,33] However, **M20**, **M40**, and **M60** appeared to be more suitable for cell attachment. The flattened cells spread with numerous filopodia, lamellipodia, and cytoplasmic extensions on these membranes. Most importantly, increased cell proliferation was found with the increase of n-HA ratio in the membranes. More continuous cell layers were formed on **M40** and **M60** substrates than that of **M0** and **M20**. These results were confirmed by MTT assay. As shown in Figure 6c, there was no significant difference in cell

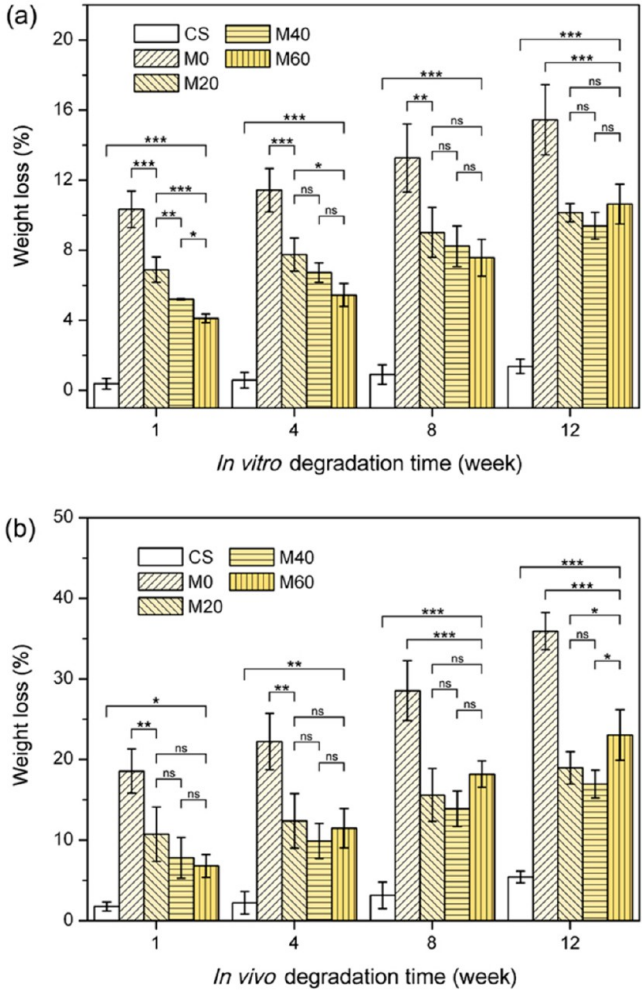

Figure 5. Weight loss of different membranes at designed degradation time: (a) in vitro degradation in PBS and (b) in vivo degradation in the back muscles of SD rats. (Error bars represent standard deviation from the mean (n = 3). ***: p<0.001. **: p<0.01. *: p<0.05. ns (no significant difference): p > 0.05.)

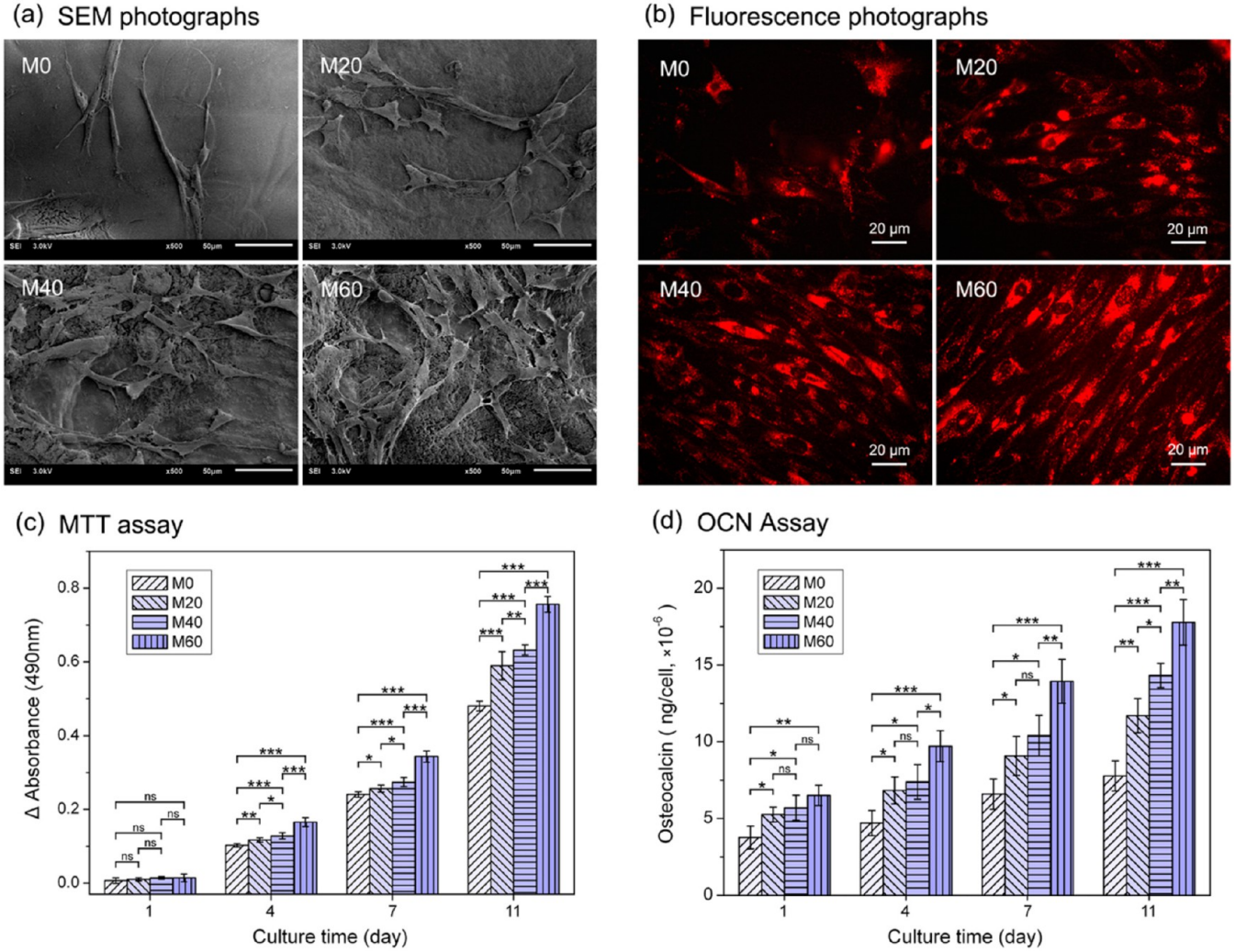

Figure 6. (a) SEM photographs at 7 days, (b) fluorescence images at 7 days, (c) MTT, and (d) OCN assay of osteoblasts cultured on the hybrid membranes. (Error bars represent standard deviation from the mean ($n = 3$). ***: $p < 0.001$. **: $p < 0.01$. *: $p < 0.05$. ns (no significant difference): $p > 0.05$.)

viability at initial period of culture. But 4 days later, cell viability was enhanced with the increase of n-HA ratio in the membrane. The cells seeded on **M60** showed the highest cell viability compared with **M0**, **M20**, and **M40**. This trend continued in the following culture periods. Osteocalin (OCN) expression of osteoblasts cultured on the membranes was shown in Figure 6d. As can be seen from the bar chart, the OCN level increased with the increase of n-HA ratio in the membrane, and the cells seeded on **M60** showed the highest level of OCN expression.

3.4. Mechanical Properties of the Spiral-Cylindrical Scaffold. The scaffold exhibited a compressive strength of 4.91 ± 0.54 MPa, which was comparable to that of cancellous bone (1−12 MPa).[34]

3.5. In Vivo Osteogenesis of the Spiral-Cylindrical Scaffold. Figure 7a showed the typical X-ray images of the surgical site at different implantation time. An opaque calcified shadow was observed at the bone-implant interface 4 weeks after surgery, but the density of the implant was lower than normal tissues. Eight weeks later, calcification became evident at the implant site, and callus formed around the periphery of the scaffold as well as along the adjacent host bone surface. Radiopacity was observed in the whole implant bridging both ends of the defect at 12 weeks, implying that new bone tissue grew through the entire scaffold and remodelled into cortical bone. The defect of the control group also gradually cicatrized with time, but the newly formed bone was slightly thinner than the normal radius. Figure 7b showed the 3D reconstructed images of the surgical site at rabbit radius. Limited amount of new bone generated at the periphery of the implant at 4 weeks, and clear suture marks were observed on the scaffold and cortical bone surface. At 8 weeks post-surgery, callus formed at both ends of the scaffold and the suture marks faded away. The regenerated bone tissue tightly integrated with the scaffold at 12 weeks, a large area of the scaffold surface was wrapped with new bone tissue. For the control group, the edges of the radius defect became smooth with time due to callus formation. But the defect was not fully reconstructed at 12 weeks as evidenced by a slight concave surface in the middle part of the radius. To evaluate bone regeneration inside the scaffold, a cylindrical region of interest (ROI) was chosen for quantitative analysis (only for the scaffold group). The detailed information on structural parameters was shown in Figure 7c. Bone volume density (bone volume/tissue volume, BV/TV) and bone mineral density (BMD) were significantly increased with time. On the contrary, bone surface density (bone surface area/bone volume, BS/BV) showed a downward trend, which

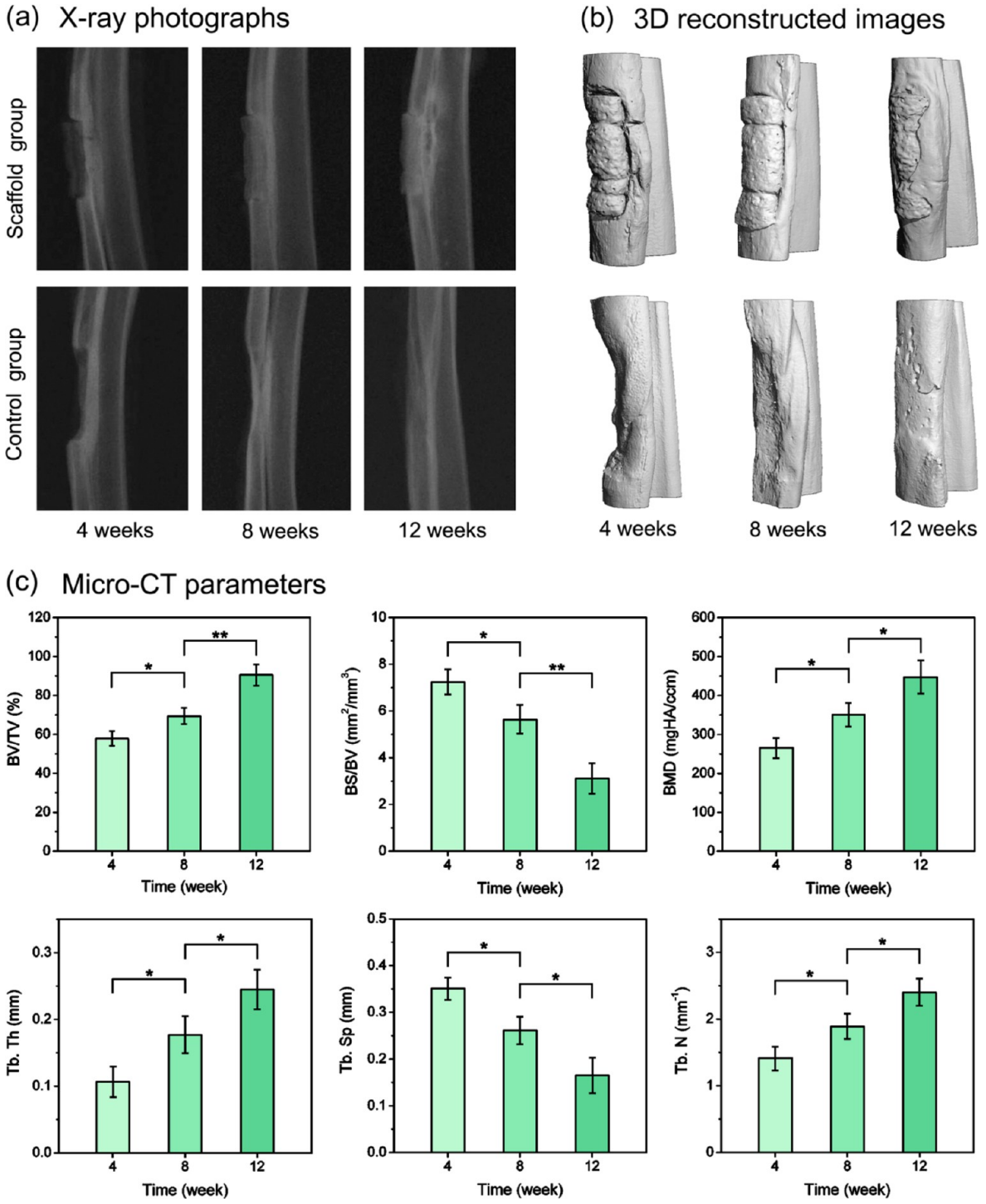

Figure 7. (a) X-ray photographs and (b) 3D reconstructed images of rabbit forelimb bone, and (c) micro-CT parameters of new bone formation inside the spiral-cylindrical scaffold (only for the scaffold group). (Error bars represent standard deviation from the mean (n = 3). **: p<0.01. *: p<0.05.)

indicated that the new formed bone gradually grew into the scaffold. Moreover, the increase of trabecular thickness (TbTh) and trabecular number (TbN) as well as the decline of trabecular separation (TbSp) also confirmed the bone regeneration.

To detect whether the bone tissue grew throughout the entire spiral-cylindrical scaffold, cross sections in the middle of the scaffold were assessed by histological observation (only for the scaffold group). As shown in Figure 8a and d, the spiral scaffold was surrounded by a fibrotic tissue layer at 4 weeks, this can be considered part of the normal response of the host. The fibrotic capsule degraded at 8 weeks (Figure 8b), and the newly generated bone tissues spread along the spiral wall of the scaffold (Figure 8e). Moreover, bone marrow was observed in the central part and among the membrane layers of the spiral cylinder (Figure 8a and b). It confirmed that the spiral-cylindrical structure allowed bone marrow flow. At 12 weeks, the new bone tissues wrapped around the scaffold and grown

dx.doi.org/10.1021/am4038432 | ACS Appl. Mater. Interfaces 2013, 5, 12036−12044

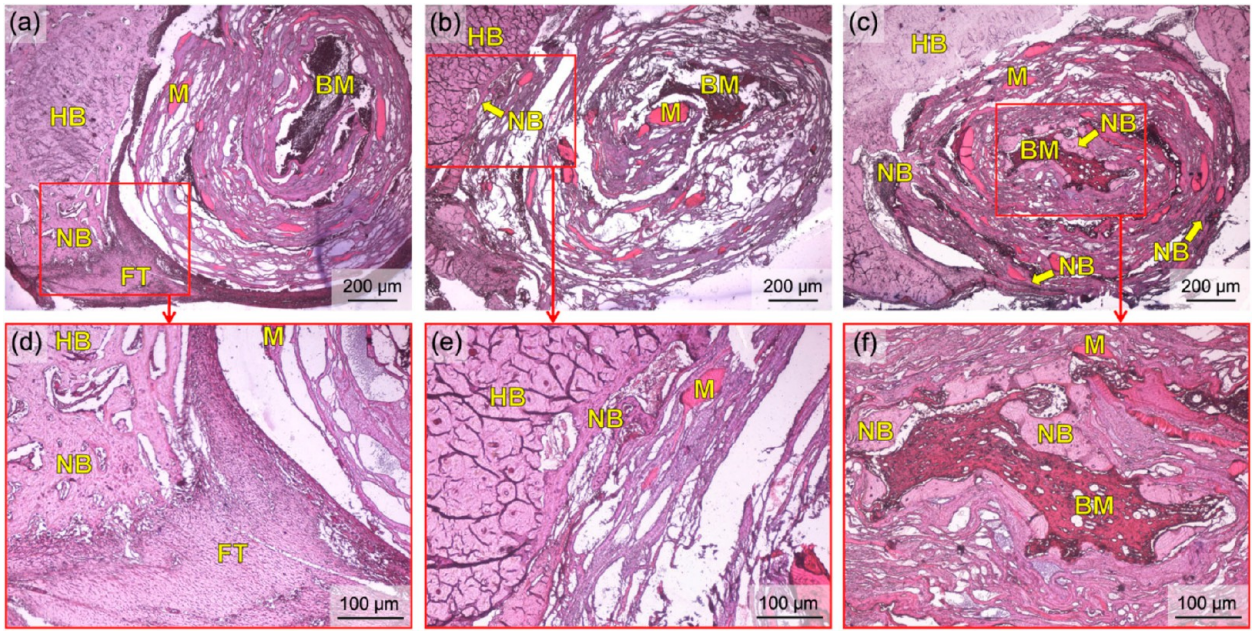

Figure 8. Histological sections of the scaffold at 4 (a, d), 8 (b, e), and 12 weeks (c, f) post-implantation. (HB: host bone. NB: new bone. FT: fibrotic tissue. BM: bone marrow. M: material.)

into the spiral structure, evidenced by a great amount of woven bone and bone trabecula formed along the spiral wall and tightly integrated with the scaffold (Figure 8c). Most importantly, the regenerated bone tissues formed a medullary cavity in the center of the spiral material, abundant bone marrow was observed filling in the cavitary space (Figure 8f).

4. DISCUSSION

The hybrid CS/CMC/n-HA membrane was formed by gradual electrostatic assembly. During the process, the extended cationic CS chains bond with surrounding anionic CMC chains through electrostatic interaction and hydrogen bonding forming a polymer matrix framework, in which the n-HA crystals also formed hydrogen bonds with the polymer chains and helped to promote the stability of the membrane (see the Supporting Information, Figure S2). The n-HA crystals contain a large amount of hydrophilic groups (−OH). With the increase of n-HA, the number of −OH on the membrane surface grew accordingly, and the hydrophilicity of the membrane could be increased. This hypothesis was confirmed by water contact angle assay. **M0**, **M20**, and **M40** exhibited water contact angles higher than 65° implying their hydrophobic surface property, **M60** showed a water contact angle of 54.37 ± 4.50° lower than that of the typical hydrophobic surface (>65°).[35] With a moderate hydrophilic surface, **M60** was considered to be more favorable for cell adhesion and proliferation than other hydrophobic membranes.[36] In addition, the membranes showed a decline in swelling degree due to the increase of n-HA and decrease of CS and CMC ratio. Besides, the increased intermolecular hydrogen bonds between n-HA and polysaccharides also made a more compact polymer matrix. The decrease of swelling degree could prevent the material from serious deformation. When used as bone repair material, this property is helpful for providing sufficient mechanical support for the host bone before new bone formation. On the basis of the above mentioned results, we concluded that **M60** was better than the other membranes for scaffold fabrication.

The repairing process of bone defects could take several weeks or even longer. In this process, the scaffold has to provide temporary mechanical support before new tissue regeneration, and meanwhile it should be gradually absorbed or metabolized in vivo. Thus it is important to regulate the balance between scaffold degradation and new bone formation. Since our scaffold was fabricated using the hybrid CS/CMC/n-HA membrane, the degradation behaviors of the membranes were carefully evaluated. The results showed that the in vivo degradation level was higher than in vitro for all the membranes. This was because the degradation of CS and CMC was primarily attributed to enzyme hydrolysis, and the existence of in vivo hydrolysis enzymes (such as such as lysozyme, proteases, and lipases[37,38]) accelerated the cleavage of β-(1-4) glycosidic bounds in CS and CMC.[37,39,40] Moreover, the combination of CMC with CS could greatly improve the degradation rate of CS membrane, and the addition of n-HA could slow down the degradation of CS/CMC membrane. This was due to the existence of strong hydrogen bonds between n-HA and polysaccharides, which regulated the structure stability of the hybrid membrane. It should be noted that, the network was stable only within a certain range of n-HA, when the n-HA ratio increased to 60 wt %, the polymer matrix could not remain long-term stable, and the degradation accelerated in the later period. During the process, calcium ion and inorganic phosphate gradually released into the surrounding environment, which could be benefit for the reconstruction of bone defect.[41] Moreover, the irregular holes appeared on **M60** with pore size larger than 100 μm were helpful for bone ingrowth into porous scaffold.[17] These degradation behaviors suggested that **M60** was better than other membrane for scaffold fabrication.

In the literature, there are some reports that demonstrate the inhibitory effect of hydroxyapatite nanoparticles on the proliferation of cells.[42,43] However, hydroxyapatite in the form of coating or composite has been confirmed to promote osteoblast proliferation and differentiation, as well as bone reconstruction.[44−47] Our experiment also gave a positive result

that n-HA in the hybrid membrane do enhance cell adhesion, spreading, proliferation and differentiation. The membranes with higher n-HA ratio exhibited better cellular compatibility. According to the previous report, n-HA have high osteoconductivity and bioactivity, as well as excellent biocompatibility with hard tissues.[48−50] Besides, the membranes with higher n-HA ratio are much rougher and more hydrophilic than the lower ones. These properties resulted in the enhancement of cell proliferation and phenotype expression on the membranes with higher n-HA ratio. Compared with other membranes, **M60** (60 wt % n-HA) was most favorable for cell growth, thus it was used to fabricate the spiral-cylindrical scaffold.

Besides the biodegradability and biocompatibility, the mechanical property of the implant also plays an important role in bone reconstruction. According to our previous study, the tensile strength of **M60** membrane was 2.38 ± 0.11 Mpa.[23] After curling it in a concentric manner to generate an anisotropic spiral cylinder, the scaffold exhibited sufficient compressive strength (~4.91 MPa) to support new bone regeneration at the site of implantation.[34]

Osteogenesis capability of the spiral-cylindrical scaffold was evaluated in a concave radius defect model of rabbit. Both X-ray photographs and 3D micro-CT analysis showed that, new formed bone wrapped around the scaffold and grew into the spiral-cylindrical structure. Because the animal model was a non-critical-sized defect, bone regeneration was also observed in the control group. However, in many cases when the bone defect is too severe or the local environment conditions are not adequate for self-repair, the bone-repairing scaffolds are necessary for healing these defects.[51] In this experiment, the n-HA ratio of the scaffold (60 wt %) was similar to that of natural bone (around 65 wt %),[52] which was helpful for implant osteointegration. With the degradation of the material, the scaffold could be tightly integrated with newly formed bone tissue. Histological sections showed the details of bone regeneration inside the spiral-cylindrical scaffold. At the initial stage after surgery, the implantation of biodegradable materials would activate humoral and cellular mechanisms to produce inflammatory and healing responses of the foreign objects.[53] The inflammatory cells, including leukocytes, monocytes and lymphocytes faded away 4 weeks after surgery, but the fibroblasts still gathered around the material. This can be considered part of the normal process of response of the host after implantation. Subsequent degradation of fibrotic layer and infiltration of regenerated bone tissues revealed that the scaffold was highly biocompatible. Since the scaffold architecture consisted of a porous surface and a spiral-cylindrical channel, bone would be forming not only from the margins but also throughout the whole space of the scaffold, this discontinuous bone ingrowth could result in faster healing than continuous ingrowth.[19,54] Most importantly, bone marrow was observed inside the the spiral-cylindrical scaffold. This was critical for bone tissue regeneration since the bone marrow was rich of mesenchymal stem cells and osteoblasts.[55,56] Bone marrow penetrated the spiral cylinder and eventually formed a medullary cavity in the center of the scaffold, which demonstrated that the spiral-cylindrical scaffold could guide oriented bone regeneration throughout the entire implant in vivo, leading to successful bone integration and regeneration.

5. CONCLUSION

The biomimetic spiral-cylindrical scaffold was developed based on hybrid CS/CMC/n-HA membrane for bone regeneration. After assessment of physicochemical characteristics, degradation behaviour, and cellular compatibility, the optimized hybrid membrane exhibited a rough and moderate hydrophilic surface, controllable degradation behaviour, and provided excellent microenvironment for osteoblast adhesion, proliferation and differentiation. In vivo evaluation demonstrated that the spiral-cylindrical architecture could promote complete infiltration of bone tissue throughout the entire scaffold. New bone tissues grew along the spiral wall bridging both ends of the defect, bone marrow penetrated the entire spiral cylinder and formed a medullary cavity in the center of the scaffold, leading to successful osteointegration and functional reconstruction. Taken together, the fabricated scaffold has a potential for the treatment of large bone defects, and the capability of the scaffold for healing of critical-sized segmental bone defects is currently under investigation.

■ ASSOCIATED CONTENT

Supporting Information

Experimental details and characterization data. This material is available free of charge via the Internet at http://pubs.acs.org.

■ AUTHOR INFORMATION

Corresponding Authors

*E-mail: nic7504@scu.edu.cn. Tel: +86 28 85412847. Fax: +86 28 85417273.

*E-mail: xcyang@tmmu.edu.cn. Tel.: +86 23 68772482. Fax: +86 23 68772482.

Author Contributions

H.J. and Y.Z. contributed equally to this work.

Notes

The authors declare no competing financial interest.

■ ACKNOWLEDGMENTS

This work is supported by China-Netherlands Program Strategic Alliances (No. 2008DFB50120), 863 National Key Project (No. 2011AA030102), Sichuan Project (No. 2012FZ0125), and National Key Technology Research and Development Program of China (2012BAI42G01). The authors would like to thank Wei Zheng from School of Biomedical Engineering and Weijun Chen from The Key Laboratory of Biomechanics under the Educational Committee in Chongqing, Third Military Medical University, for the assistance in images progressing and mechanical testing.

■ REFERENCES

(1) Holzwarth, J. M.; Ma, P. X. *Biomaterials* **2011**, *32*, 9622−9629.

(2) Bongio, M.; van den Beucken, J. J.; Leeuwenburgh, S. C.; Jansen, J. A. *J. Mater. Chem.* **2010**, *20*, 8747−8759.

(3) Wang, H.; Hansen, M. B.; Löwik, D. W. P. M.; van Hest, J.; Li, Y.; Jansen, J. A. *Adv. Mater.* **2011**, *23*, H119−H124.

(4) Wang, H.; Boerman, O. C.; Sariibrahimoglu, K.; Li, Y.; Jansen, J. A.; Leeuwenburgh, S. C. G. *Biomaterials* **2012**, *33*, 8695−8703.

(5) Vallet-Regi, M.; Ruiz-Hernandez, E. *Adv. Mater.* **2011**, *23*, 5177−5218.

(6) Petite, H.; Viateau, V.; Bensaid, W.; Meunier, A.; De Pollak, C.; Bourguignon, M. *Nat. Biotechnol.* **2000**, *18*, 959−963.

(7) Kolambkar, Y. M.; Dupont, K. M.; Boerckel, J. D.; Huebsch, N.; Mooney, D. J.; Hutmacher, D. W. *Biomaterials* **2011**, *32*, 65.

(8) Vallet-Regí, M.; Colilla, M.; González, B. *Chem. Soc. Rev.* **2011**, *40*, 596−607.

(9) Zhai, H.; Jiang, W.; Tao, J.; Lin, S.; Chu, X.; Xu, X. *Adv. Mater.* **2010**, *22*, 3729−3734.

(10) Lu, L.; Zhang, X.; Wang, Y.; Ortiz, L.; Mao, X.; Jiang, Z.; Xiao, Z.; Huang, N. *ACS Appl. Mater. Interfaces* **2013**, *5*, 319−330.
(11) Wang, G.; Zheng, L.; Zhao, H.; Miao, J.; Sun, C.; Liu, H.; Huang, Z.; Yu, X.; Wang, J.; Tao, X. *ACS Appl. Mater. Interfaces* **2011**, *3*, 1692−1701.
(12) Mizrahy, S.; Peer, D. *Chem. Soc. Rev.* **2012**, *41*, 2623−2640.
(13) Darder, M.; Aranda, P.; Ferrer, M. L.; Gutiérrez, M. C.; del Monte, F.; Ruiz-Hitzky, E. *Adv. Mater.* **2011**, *23*, 5262−5267.
(14) Frohbergh, M. E.; Katsman, A.; Botta, G. P.; Lazarovici, P.; Schauer, C. L.; Wegst, U. G. K. *Biomaterials* **2012**, *33*, 9167−9178.
(15) Fang, B.; Wan, Y. Z.; Tang, T. T.; Gao, C.; Dai, K. R. *Tissue Eng., Part A* **2009**, *15*, 1091−1098.
(16) Zhao, L.; Weir, M. D.; Xu, H. H. K. *Biomaterials* **2010**, *31*, 6502−6510.
(17) Langer, R.; Vacanti, J. P. *Science* **1993**, *260*, 920−926.
(18) Li, X.; Zhao, Y.; Bing, Y.; Li, Y.; Gan, N.; Guo, Z.; Peng, Z.; Zhu, Y. *ACS Appl. Mater. Interfaces* **2013**, *5*, 5557−5562.
(19) Karageorgiou, V.; Kaplan, D. *Biomaterials* **2005**, *26*, 5474−6491.
(20) Erli, H. J.; Rüger, M.; Ragoß, C.; Jahnen-Dechent, W.; Hollander, D. A.; Paar, O. *Biomaterials* **2006**, *27*, 1270−1276.
(21) Liu, X.; Wu, S.; Yeung, K. W.; Chan, Y.; Hu, T.; Xu, Z. *Biomaterials* **2011**, *32*, 330−338.
(22) Weiner, S.; Wagner, H. D. *Annu. Rev. Mater. Sci.* **1998**, *28*, 271−298.
(23) Jiang, H.; Zuo, Y.; Cheng, L.; Wang, H.; Gu, A.; Li, Y. *J. Mater. Sci.: Mater. M.* **2011**, *22*, 289−297.
(24) Zuo, Y.; Xiao, W.; Chen, X.; Tang, Y.; Luo, H.; Fan, H. *Chem. Commun.* **2012**, *48*, 3170−3172.
(25) Deng, M.; Kumbar, S. G.; Nair, L. S.; Weikel, A. L.; Allcock, H. R.; Laurencin, C. T. *Adv. Funct. Mater.* **2011**, *21*, 2641−2651.
(26) Wang, J.; Valmikinathan, C. M.; Liu, W.; Laurencin, C. T.; Yu, X. *J. Biomed. Mater. Res. A* **2010**, *93*, 753−762.
(27) Wang, J.; Yu, X. *Acta Biomater.* **2010**, *6*, 3004.
(28) Wang, J.; Shah, A.; Yu, X. *Mater. Sci. Eng., C* **2011**, *31*, 50−56.
(29) Sima, Z.; Wu, J. *Cell Culture*; World Publishing Corporation: Xi'an, China, 2007; p 57−59.
(30) Cao, Y. *The Theory and Practice of Tissue Engneering*; Shanghai Scientific & Technical Publishers: Shanghai, China, 2004; p 106−107.
(31) Jones, S.; Boyde, A. *Cell Tissue Res.* **1977**, *184*, 179−193.
(32) Yeong, W. Y.; Chua, C. K.; Leong, K. F.; Chandrasekaran, M. *Trends Biotechnol.* **2004**, *22*, 643−652.
(33) Landers, R.; Hübner, U.; Schmelzeisen, R.; Mülhaupt, R. *Biomaterials* **2002**, *23*, 4437−4447.
(34) Vuola, J.; Taurio, R.; Göransson, H.; Asko-Seljavaara, S. *Biomaterials* **1998**, *19*, 223−227.
(35) Herrwerth, S.; Eck, W.; Reinhardt, S.; Grunze, M. *J. Am. Chem. Soc.* **2003**, *125*, 9359−9366.
(36) Marques, A.; Reis, R.; Hunt, J. *Biomaterials* **2002**, *23*, 1471−1478.
(37) Kean, T.; Thanou, M. *Adv. Drug. Delivery Rev* **2010**, *62*, 3−11.
(38) Jeon, Y. J.; Kim, S. K. *Carbohydr. Polym.* **2000**, *41*, 133−141.
(39) Zhang, Y. H. P.; Lynd, L. R. *Biotechnol. Bioeng.* **2004**, *88*, 797−824.
(40) Vishu Kumar, A.; Tharanathan, R. *Carbohydr. Polym.* **2004**, *58*, 275−283.
(41) Kim, H. W.; Kim, H. E.; Salih, V. *Biomaterials* **2005**, *26*, 5221−5230.
(42) Chen, L.; Mccrate, J. M.; Lee, J. C.; Li, H. *Nanotechnology* **2011**, *22*, 105708.
(43) Tang, W.; Yuan, Y.; Liu, C.; Wu, Y.; Lu, X.; Qian, J. *Nanomedicine* **2013**, DOI: 10.2217/nnm.12.217.
(44) Dinarvand, P.; Seyedjafari, E.; Shafiee, A.; Babaei-Jandaghi, A.; Doostmohammadi, A.; Fathi, M. H.; Farhadian, S.; Soleimani, M. *ACS Appl. Mater. Interfaces* **2011**, *3*, 4518−4524.
(45) Cicuéndez, M.; Izquierdo-Barba, I.; Sánchez-Salcedo, S.; Vila, M.; Vallet-Regí, M. *Acta Biomater.* **2012**, *8*, 802−810.
(46) Sailaja, G.; Ramesh, P.; Kumary, T.; Varma, H. *Acta Biomater.* **2006**, *2*, 651−657.
(47) Li, M.; Liu, W.; Sun, J.; Xianyu, Y.; Wang, J.; Zhang, W.; Zheng, W.; Huang, D.; Di, S.; Long, Y. *ACS Appl. Mater. Interfaces* **2013**, *5*, 5921−5926.
(48) Shen, Z.; Adolfsson, E.; Nygren, M.; Gao, L.; Kawaoka, H.; Niihara, K. *Adv. Mater.* **2001**, *13*, 214−216.
(49) Zhou, H.; Lee, J. *Acta Biomater.* **2011**, *7*, 2769−2781.
(50) Bhumiratana, S.; Grayson, W. L.; Castaneda, A.; Rockwood, D. N.; Gil, E. S.; Kaplan, D. L. *Biomaterials* **2011**, *32*, 2812−2820.
(51) Tiainen, H.; Wohlfahrt, J. C.; Verket, A.; Lyngstadaas, S. P.; Haugen, H. J. *Acta Biomater.* **2012**, *8*, 2384−2391.
(52) Wang, X.; Li, Y.; Wei, J.; de Groot, K. *Biomaterials* **2002**, *23*, 4787−4791.
(53) Sastre, R. L.; Olmo, R.; Teijón, C.; Muñíz, E.; Teijón, J. M.; Blanco, M. D. *Int. J. Pharm.* **2007**, *338*, 180−190.
(54) Simon, J. L.; Roy, T. D.; Parsons, J. R.; Rekow, E. D.; Thompson, V. P.; Kemnitzer, J. *J. Biomed. Mater. Res. A* **2003**, *66*, 275−282.
(55) Chamberlain, G.; Fox, J.; Ashton, B.; Middleton, J. *Stem Cells* **2007**, *25*, 2739−2749.
(56) Zhou, S.; Greenberger, J. S.; Epperly, M. W.; Goff, J. P.; Adler, C.; LeBoff, M. S. *Aging Cell* **2008**, *7*, 335−343.